Time Dependent Adjoint-based Optimization for Coupled Aeroelastic Problems

Asitav Mishra * Karthik Mani † Dimitri Mavriplis ‡

Jay Sitaraman §

Department of Mechanical Engineering,University of Wyoming, Laramie, WY 82071-3295.

A formulation for sensitivity analysis of fully coupled time-dependent aeroelastic problems is given in this paper. Both forward sensitivity and adjoint sensitivity formulations are derived that correspond to analogues of the non-linear aeroelastic analysis problem. Both sensitivity analysis formulations make use of the same iterative disciplinary solution techniques used for analysis, and make use of an analogous coupling strategy. The information passed between fluid and structural solvers is dimensionally equivalent in all cases, enabling the use of the same data structures for analysis, forward and adjoint problems. Sensitivities from both forward and adjoint formulations for the fully coupled aeroelastic problem are verified using the complex step method and agreement to machine precision is demonstrated. The fully coupled adjoint formulation is then used to perform rotor blade design optimization on a Hart2 rotor in hover while constraining the time-integrated thrust coefficient to the baseline value. The optimized rotor achieves 2% reduced torque with a penalty of 1% reduction of thrust.

I. Introduction

In the recent past, the use of adjoint equations has become a popular approach for solving aerodynamic design optimization problems based on computational fluid dynamics (CFD).[1–6] Adjoint equations are a very powerful tool in the sense that they allow the computation of sensitivity derivatives of an objective function to a set of given inputs at a cost which is essentially independent of the number of inputs. This is in contrast to the brute-force finite-difference method, where each input or design variable has to be perturbed individually to obtain a corresponding effect on the output. This is a tedious and costly process which is of little use when there are a large number of design variables or inputs. Another major shortcoming of the finite-difference method is that it suffers from step-size limitations which affect the accuracy of the computed gradients.

While the use of adjoint equations is now fairly well established in steady-state shape optimization, only recently have inroads been made into extending them to unsteady flow problems. Unsteady discrete adjoint-based shape optimization was initially demonstrated in the context of two-dimensional problems by Mani and Mavriplis[7] and also by Rumpfkeil and Zingg.[8] Preliminary demonstration of the method's feasibility in three-dimensional problems was done by Mavriplis.[9] Full implementation in a general sense and application to large scale problems involving helicopter rotors was then carried out by Nielsen et.al. in the NASA FUN3D code.[10,11]

Since engineering optimization is an inherently multidisciplinary endeavor, the next logical step involves extending adjoint methods to multidisciplinary simulations and using the obtained sensitivities for driving multidisciplinary optimizations. In the context of fixed and especially rotory wing aircraft, aeroelastic coupling effects can be very important and must be considered in the context of a successful optimization strategy.

The coupling of computational fluid dynamics (CFD) and computational structural dynamics (CSD) and the use of sensitivity analysis on such a system has been addressed in the past primarily from a steady-state standpoint. Until now, relatively little work has been done addressing unsteady aeroelastic optimization problems, mainly due to complexities in the linearization of coupled time-dependent systems. In previous work, we have derived the fully coupled adjoint

*Postdoctoral Research Associate; amishra3@uwyo.edu

†Associate Research Scientist; kmani@uwyo.edu

‡Professor; mavripl@uwyo.edu

§Assistant Professor; jsitaram@uwyo.edu

problem for a two-dimensional aeroelastic airfoil problem and demonstrated the use of adjoint-derived sensitivities for performing time-dependent aeroelastic optimization including flutter suppression.[12]

The objective of the current work is to extend the previously developed time-dependent aerodynamic adjoint-based optimization capability[13] to include fully coupled aero-structural dynamics effects for three dimensional flexible rotor design. The structural deformations are obtained using a Hodges-Dowell type beam finite-element based solver with adjoint formulation for computing functional sensitivities to aerodynamic and structural design variables. The CFD solver used is a 3-D Navier-Stokes Unstructured (NSU3D) finite-volume code, which has previously been extended to include a steady[14] and unsteady[15] discrete adjoint capability. The following sections describe the formulation and validation of each disciplinary component of the combined aero-structural analysis and sensitivity problems, as well as the coupling of these components to form the coupled aero-structural optimization capability.

II. Aerodynamic Analysis and Sensitivity Formulation

II.A. Flow Solver Analysis Formulation

The base flow solver used in this work is the NSU3D unstructured mesh Reynolds-averaged Navier-Stokes solver. NSU3D has been widely validated for steady-state and time-dependent flows and contains a discrete tangent and adjoint sensitivity capability which has been demonstrated previously for optimization of steady-state and time-dependent flow problems. As such, only a concise description of these formulations will be given in this paper, with additional details available in previous references.[13–15] The flow solver is based on the conservative form of the Navier-Stokes equations which may be written as:

$$\frac{\partial \mathbf{U}(\mathbf{x},t)}{\partial t} + \nabla \cdot \mathbf{F}(\mathbf{U}) = 0 \tag{1}$$

For moving mesh problems these are written in arbitrary Lagrangian-Eulerian (ALE) form as:

$$\frac{\partial V\mathbf{U}}{\partial t} + \int_{dB(t)} [\mathbf{F}(\mathbf{U}) - \dot{\mathbf{x}}\mathbf{U}] \cdot \mathbf{n} dB = 0 \tag{2}$$

Here V refers to the area of the control volume, $\dot{\mathbf{x}}$ is the vector of mesh face or edge velocities, and $\mathbf{n}$ is the unit normal of the face or edge. The state vector $\mathbf{U}$ consists of the conserved variables and the cartesian flux vector $\mathbf{F} = (\mathbf{F}_x, \mathbf{F}_y, \mathbf{F}_z)$ contains both inviscid and viscous fluxes. The equations are closed with the perfect gas equation of state and the Spalart-Allmaras turbulent eddy viscosity model[16] for all cases presented in this work.

The solver uses a vertex-centered median dual control volume formulation that is second-order accurate, where the inviscid flux integral S around a closed control volume is discretized as:

$$S = \int_{dB(t)} [\mathbf{F}(\mathbf{U}) - \dot{\mathbf{x}}\mathbf{U}] \cdot \mathbf{n} dB = \sum_{i=1}^{n_{edge}} \mathbf{F}_{e_i}^{\perp}(V_{e_i}, \mathbf{U}, \mathbf{n}_{e_i}) B_{e_i} \tag{3}$$

where B_e is the face area, V_e is the normal face velocity, $\mathbf{n}_e$ is the unit normal of the face, and $F_e^{\perp}$ is the normal flux across the face. The normal flux across the face is computed using the second-order accurate matrix dissipation scheme[17] as the sum of a central difference and an artificial dissipation term as shown below,

$$\begin{aligned} \mathbf{F}_e^{\perp} &= \frac{1}{2}\{\mathbf{F}_L^{\perp}(\mathbf{U}_L, V_e, \mathbf{n}_e) + \mathbf{F}_R^{\perp}(\mathbf{U}_R, V_e, \mathbf{n}_e) \\ &\quad + \kappa^{(4)}[T]|[\lambda]|[T]^{-1}\left\{(\nabla^2\mathbf{U})_L - (\nabla^2\mathbf{U})_R\right\}\} \end{aligned} \tag{4}$$

where $\mathbf{U}_L$, $\mathbf{U}_R$ are the left and right state vectors and $(\nabla^2\mathbf{U})_L$, $(\nabla^2\mathbf{U})_R$ are the left and right undivided Laplacians computed for any element i as

$$(\nabla^2\mathbf{U})_i = \sum_{k=1}^{neighbors} (\mathbf{U}_k - \mathbf{U}_i) \tag{5}$$

The time derivative term is discretized using a second-order accurate backward-difference formula (BDF2) scheme as:

$$\frac{\partial V\mathbf{U}}{\partial t} = \frac{\frac{3}{2}V^n\mathbf{U}^n - 2V^{n-1}\mathbf{U}^{n-1} + \frac{1}{2}V^{n-2}\mathbf{U}^{n-2}}{\Delta t} \tag{6}$$

The index n is used to indicate the current time-level as the convention throughout the paper. The discretization of the BDF2 scheme shown in equation (6) is based on a uniform time-step size.

Denoting the spatially discretized terms at time level n by the operator $S^n(\mathbf{U}^n)$, the resulting system of non-linear equations to be solved for the analysis problem at each time step can be written as:

$$\mathbf{R}^n = \frac{\frac{3}{2}V^n\mathbf{U}^n - 2V^{n-1}\mathbf{U}^{n-1} - \frac{1}{2}V^{n-2}\mathbf{U}^{n-2}}{\Delta t} + S^n(\mathbf{U}^n) = 0 \tag{7}$$

which in simplified form exhibiting the functional dependencies on $\mathbf{U}$ and $\mathbf{x}$ at different time levels is given as:

$$\mathbf{R}^n(\mathbf{U}^n, \mathbf{U}^{n-1}, \mathbf{U}^{n-2}, \mathbf{x}^n, \mathbf{x}^{n-1}, \mathbf{x}^{n-2}) = 0 \tag{8}$$

At each time step n, the implicit residual is linearized with respect to the unknown solution vector $\mathbf{U}^n$ and solved for using Newton's method as:

$$\begin{gathered}\left[\frac{\partial \mathbf{R}^k}{\partial \mathbf{U}^k}\right]\delta\mathbf{U}^k = -\mathbf{R}^k \\ \mathbf{U}^{k+1} = \mathbf{U}^k + \delta\mathbf{U}^k \\ \delta\mathbf{U}^k \to 0, \mathbf{U}^n = \mathbf{U}^k\end{gathered} \tag{9}$$

The Jacobian matrix is inverted iteratively using a line-implicit agglomeration multigrid scheme that can also be used as a preconditioner for a GMRES Krylov solver.[18]

Although the above equation denotes the solution at a single time level n, for the remainder of this paper we will use the generalized notation:

$$\mathbf{R}(\mathbf{U}, \mathbf{x}) = 0 \tag{10}$$

where the vector $\mathbf{U}$ denotes the flow values at all time steps, and where each (block) row in this equation corresponds to the solution at a particular time step as given in equation (8). Equation (10) denotes the simultaneous solution of all time steps and is solved in practice by Newton's method using forward block substitution (i.e. forward integration in time) since each new time step depends on the previous two time levels.

II.B. Mesh deformation capability

In order to deform the mesh for time-dependent problems a spring analogy and a linear elastic analogy mesh deformation approach have been implemented. The linear elasticity approach has proven to be much more robust and is used exclusively in this work. In this approach, the mesh is modeled as a linear elastic solid with a variable modulus of elasticity that can be prescribed either as inversely proportional to cell volume or to the distance of each cell from the nearest wall.[19,20] The resulting equations are discretized and solved on the mesh in its original undeformed configuration in response to surface displacements using a line-implicit multigrid algorithm analogous to that used for the flow equations. The governing equations for mesh deformation can be written symbolically as:

$$\mathbf{G}(\mathbf{x}, \mathbf{D}) = \mathbf{0} \tag{11}$$

where $\mathbf{x}$ denotes the interior mesh coordinates and $\mathbf{D}$ denotes shape parameters that define the surface geometry.

III. Aerodynamic Sensitivity Analysis Formulation

The basic sensitivity analysis implementation follows the strategy developed in references.[9,14] Consider an arbitrary objective function L that is evaluated using the unsteady flow solution set $\mathbf{U}$ and unsteady mesh solution set $\mathbf{x}$ expressed as:

$$L = L(\mathbf{U}, \mathbf{x}) \tag{12}$$

Assuming that the state variables (i.e.$\mathbf{U}, \mathbf{x}$) are dependent on some input design parameters $\mathbf{D}$, the total sensitivity of the objective function L to the set of design inputs can be expressed as the inner product between the vector of state sensitivities to design inputs and the vector of objective sensitivities to the state variables as:

$$\frac{dL}{d\mathbf{D}} = \begin{bmatrix} \frac{\partial L}{\partial \mathbf{x}} & \frac{\partial L}{\partial \mathbf{U}} \end{bmatrix} \begin{bmatrix} \frac{\partial \mathbf{x}}{\partial \mathbf{D}} \\ \frac{\partial \mathbf{U}}{\partial \mathbf{D}} \end{bmatrix} \tag{13}$$

The non-linear flow residual operator and the linear elasticity mesh residual operator as described earlier provide the constraints which can be expressed in general form over the whole space and time domains as:

$$\mathbf{G}(\mathbf{x},\mathbf{D}) = 0 \tag{14}$$

$$\mathbf{R}(\mathbf{U},\mathbf{x}) = 0 \tag{15}$$

which when linearized with respect to the design inputs yields:

$$\begin{bmatrix} \frac{\partial \mathbf{G}}{\partial \mathbf{x}} & 0 \\ \frac{\partial \mathbf{R}}{\partial \mathbf{x}} & \frac{\partial \mathbf{R}}{\partial \mathbf{U}} \end{bmatrix} \begin{bmatrix} \frac{\partial \mathbf{x}}{\partial \mathbf{D}} \\ \frac{\partial \mathbf{U}}{\partial \mathbf{D}} \end{bmatrix} = \begin{bmatrix} -\frac{\partial \mathbf{G}}{\partial \mathbf{D}} \\ 0 \end{bmatrix} \tag{16}$$

These constitute the forward sensitivity or tangent sensitivity equations. In practice these equations may be solved by forward substitution following:

$$\frac{\partial \mathbf{G}}{\partial \mathbf{x}} \frac{\partial \mathbf{x}}{\partial \mathbf{D}} = -\frac{\partial \mathbf{G}}{\partial \mathbf{D}} \tag{17}$$

$$\frac{\partial \mathbf{R}}{\partial \mathbf{U}} \frac{\partial \mathbf{U}}{\partial \mathbf{D}} = -\frac{\partial \mathbf{R}}{\partial \mathbf{x}} \frac{\partial \mathbf{x}}{\partial \mathbf{D}} \tag{18}$$

$\frac{\partial \mathbf{G}}{\partial \mathbf{D}}$ represents the sensitivity of the surface mesh points to a change in the shape parameter $\mathbf{D}$ which can be considered as a known input vector. Thus, the first equation may be solved to obtain the grid sensitivities $\frac{\partial \mathbf{x}}{\partial \mathbf{D}}$ which can then be used in the solution of the second equation to obtain the flow sensitivities $\frac{\partial \mathbf{U}}{\partial \mathbf{D}}$. In both cases, the required inversion of each disciplinary Jacobian matrix can be accomplished following the same solution procedure used for the corresponding analysis problem, i.e. following equation (9) for the flow equations. Since these equations represent the solution over the entire time domain, in practice this procedure is performed at each time step proceeding from the initial to final time step. The mesh and flow sensitivity vectors can then be substituted into equation (13) to obtain the complete sensitivity of the objective with respect to the design variable $\mathbf{D}$.

The forward sensitivity approach requires a new solution of equation (16) for each design parameter $\mathbf{D}$. On the other hand, the adjoint approach can obtain the sensitivities for any number of design inputs $\mathbf{D}$ at a cost which is independent of the number of design variables. The adjoint problem can be obtained by premultiplying equation (16) by the inverse of the large coupled matrix and substituting the resulting expression for the sensitivities into equation (13) and defining adjoint variables as the solution of the system:

$$\begin{bmatrix} \frac{\partial \mathbf{G}}{\partial \mathbf{x}}^T & \frac{\partial \mathbf{R}}{\partial \mathbf{x}}^T \\ 0 & \frac{\partial \mathbf{R}}{\partial \mathbf{U}}^T \end{bmatrix} \begin{bmatrix} \Lambda_{\mathbf{x}} \\ \Lambda_{\mathbf{U}} \end{bmatrix} = \begin{bmatrix} \frac{\partial L}{\partial \mathbf{x}}^T \\ \frac{\partial L}{\partial \mathbf{U}}^T \end{bmatrix} \tag{19}$$

where $\Lambda_{\mathbf{U}}$ and $\Lambda_{\mathbf{x}}$ are the flow and mesh adjoint variables respectively. The final objective sensitivities can be obtained as:

$$\frac{dL}{d\mathbf{D}}^T = \begin{bmatrix} \frac{\partial \mathbf{G}}{\partial \mathbf{D}}^T & 0 \end{bmatrix} \begin{bmatrix} \Lambda_{\mathbf{x}} \\ \Lambda_{\mathbf{u}} \end{bmatrix} \tag{20}$$

The adjoint system can be solved using back-substitution as:

$$\frac{\partial \mathbf{R}}{\partial \mathbf{U}}^T \Lambda_U = \frac{\partial L}{\partial \mathbf{U}}^T \tag{21}$$

$$\frac{\partial \mathbf{G}}{\partial \mathbf{x}}^T \Lambda_x = -\frac{\partial \mathbf{R}}{\partial \mathbf{x}}^T \Lambda_U + \frac{\partial L}{\partial \mathbf{x}}^T \tag{22}$$

where once again the inversion of the transposed Jacobian matrices can be accomplished using the same iterative techniques as applied to the analysis and tangent sensitivity problems. Recalling that equation (19) applies over the entire time domain, the back-substitution procedure leads to a reverse integration in time, beginning with the last physical time step and proceeding to the initial time step. A more detailed description of the complete formulation is presented in,[12] where the procedure has been used to perform aerodynamic shape optimization for a rigid rotor.

IV. Beam model: Analysis and Adjoint Optimization

A non-linear bend-twist beam model is a suitable and widely utilized structural model for slender fixed and rotary wing aircraft structures within the context of an aeroelastic problem. A bend-twist beam model, described below, has previously been developed and coupled to the NSU3D unstructured mesh Reynolds-averaged Navier-Stokes solver.[20,21]

IV.A. Beam Analysis Formulation

The non-linear governing equations of a slender beam are discretized using the Finite-element method (FEM) in space. Figure 1 shows a typical beam with 15 degrees of freedom for each element to accommodate bend wise, lag wise, axial and torsional displacements. The second order equation of motion for the beam can be expressed as:

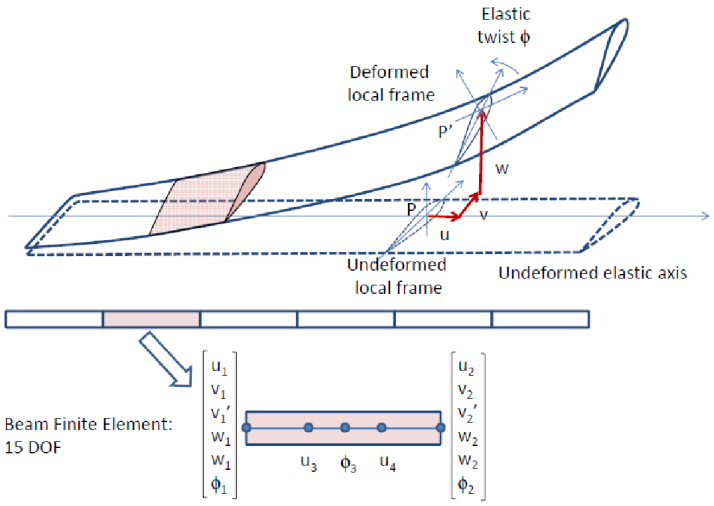

Figure 1. 15 degrees of freedom beam element with flap, lag, torsional and axial degrees of freedom.

$$[M]\ddot{\mathbf{q}} + [C]\dot{\mathbf{q}} + [K] = F \tag{23}$$

where $[M]$, $[C]$ and $[K]$ are mass, damping and stiffness matrices of the system of equations representing the beam. Vector $F = F(t)$ is the forcing vector. Vector $\mathbf{q}$ represents the displacements along all degrees of freedom. This set of equations can be reduced to a first order system and solved using a second order backward difference formula (BDF2) time integration with standard Newton-type linearization and sub-iterations to efficiently invert the implicit system:

$$[I]\dot{\mathbf{Q}} + [A]\mathbf{Q} = \mathbf{F} \tag{24}$$

where $[I]$ is the identity matrix, $\mathbf{Q} = [\mathbf{q}, \dot{\mathbf{q}}]^T$, $\mathbf{F} = [0,\ [M]^{-1}F]^T$ and $[A] = \begin{bmatrix} 0 & -[I] \\ [M]^{-1}[K] & [M]^{-1}[C] \end{bmatrix}$. The residual of the structural equations can be defined as: $\mathbf{J} = [I]\ \dot{\mathbf{Q}} + [A]\ \mathbf{Q} - \mathbf{F} = 0$, and can be expressed in a simplified form as:

$$\mathbf{J}(\mathbf{Q}, \mathbf{F}) = \mathbf{0} \tag{25}$$

The beam model has been validated for the standard Hart-2 rotor case[23] by comparing its natural frequency predictions with the predictions from other reliable CSD models. As shown in Table 1, the rotating natural frequencies compare well with those predicted by the UMARC[24] and DLR[25] structural codes, for the first 3 flap and first torsional frequency modes. Further, Fig. 2 shows that the frequency prediction over a range of operating rotor frequencies compare well with those predicted by the UMARC comprehensive code.[26]

Table 1. Comparison of Hart-II Natural Frequencies[22]

Modes	Present Model	UMARC	DLR
Flap 1	1.104	1.112	1.125
Flap 2	2.802	2.843	2.835
Flap 3	5.010	5.189	5.168
Torsion 1	3.878	3.844	3.845

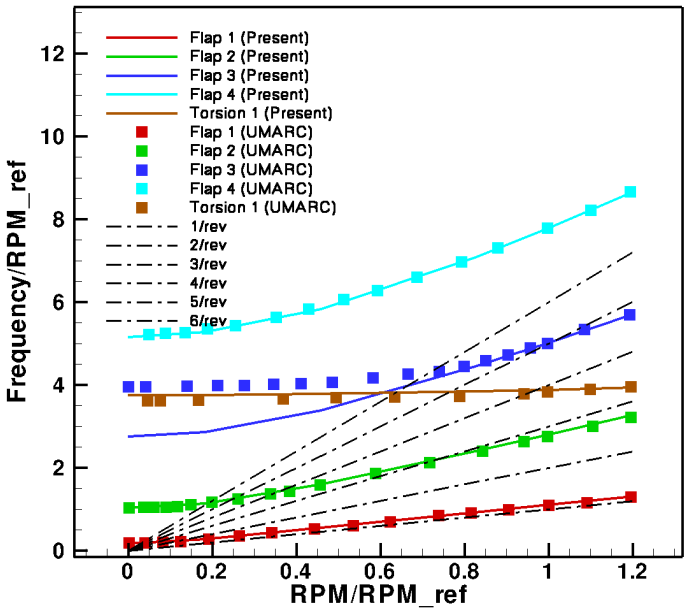

Figure 2. Fan plot comparing Beam model with UMARC[26]

IV.B. Forward Sensitivity Formulation of Beam Model

The beam tangent (forward sensitivity) linearization is similar to the analysis problem. For a given function, L, its sensitivity with respect to a blade design parameter, D can be written as: $\frac{dL}{\mathbf{dD}} = \frac{\partial L}{\partial \mathbf{D}} + \frac{\partial L}{\partial \mathbf{Q}}\frac{\partial \mathbf{Q}}{\partial \mathbf{D}}$. This requires solving for sensitivity of the beam state (Q), which can be obtained by differentiating Eqn. (25) with respect to the design variable D and rearranging as:

$$\left[\frac{\partial \mathbf{J}}{\partial \mathbf{Q}}\right]\frac{\partial \mathbf{Q}}{\partial \mathbf{D}} = -\frac{\partial \mathbf{J}}{\partial \mathbf{F}}\frac{\partial \mathbf{F}}{\partial \mathbf{D}} - \frac{\partial \mathbf{J}}{\partial \mathbf{D}} \tag{26}$$

The last term on the right hand side is non zero for structural design parameters such as beam element stiffnesses, in which case the applied force does not change with the design parameter, making the first term on the right hand size zero. In the coupled aeroelastic case, using aerodynamic shape parameters that primarily affect the airloads on the structure, the first term on the right-hand size is non-zero while the second term vanishes. Solving for $\frac{\partial \mathbf{Q}}{\partial \mathbf{D}}$ in Eqn. (26), the forward sensitivity of the objective function $\frac{dL}{d\mathbf{D}}$ can be obtained.

IV.C. Adjoint Formulation of Beam Model

The adjoint formulation of the beam model can be derived by approaching the tangent formulation in the reverse (transpose) direction. Taking the transpose of the objective functional sensitivity yields:

$$\frac{dL}{\mathbf{dD}}^T = \frac{\partial L}{\partial \mathbf{D}}^T + \frac{\partial \mathbf{Q}}{\partial \mathbf{D}}^T\frac{\partial L}{\partial \mathbf{Q}}^T \tag{27}$$

This requires solving for the transpose sensitivity of the beam state (Q). The solution of $\frac{\partial \mathbf{Q}}{\partial \mathbf{D}}^T$ can be derived from the transposed Eqn. (26):

$$\frac{\partial \mathbf{Q}}{\partial \mathbf{D}}^{\mathbf{T}} = \left[-\frac{\partial \mathbf{J}}{\partial \mathbf{D}} - \frac{\partial \mathbf{J}}{\partial \mathbf{F}}\frac{\partial \mathbf{F}}{\partial \mathbf{D}}\right]^{\mathbf{T}}\left[\frac{\partial \mathbf{J}}{\partial \mathbf{Q}}\right]^{-\mathbf{T}} \tag{28}$$

Substituting the above into Eqn. (27):

$$\frac{dL}{\mathbf{dD}}^T = \frac{\partial L}{\partial \mathbf{D}}^T + \left[-\frac{\partial \mathbf{J}}{\partial \mathbf{D}}^{\mathbf{T}} - \frac{\partial \mathbf{F}}{\partial \mathbf{D}}^{\mathbf{T}}\frac{\partial \mathbf{J}}{\partial \mathbf{F}}^{\mathbf{T}}\right]\left[\frac{\partial \mathbf{J}}{\partial \mathbf{Q}}\right]^{-\mathbf{T}}\frac{\partial L}{\partial \mathbf{Q}}^T \tag{29}$$

This requires solving for an adjoint vector $\Lambda_{\mathbf{Q}}$ defined as:

$$\left[\frac{\partial \mathbf{J}}{\partial \mathbf{Q}}\right]^T \Lambda_{\mathbf{Q}} = \frac{\partial \mathbf{L}}{\partial \mathbf{Q}}^{\mathbf{T}} \tag{30}$$

The above forms the adjoint formulation of the beam model. It is observed here again that the left hand side Jacobian term of the adjoint step is just the transpose of the Jacobian in the forward linearization. In this work, forward and adjoint formulations of the beam solver have been implemented and verified for both structural design parameters, and force-based design parameters (as required for the coupled aeroelasticity problem). The implementation includes sensitivities for both static and dynamic beam motion sensitivities. The adjoint implementation has been verified for a tip loaded (harmonically varying tip force) unsteady beam. The adjoint derived sensitivities of the beam shape due to changes in design variables, such as element stiffnesses EI, GJ, and element masses, have been shown to compare well with sensitivities computed using complex variable methods and forward sensitivity methods to within machine precision (10^{-15}).

Having established the correctness and accuracy of the structural adjoint formulation, the potential for using this approach to drive time-dependent structural optimization problems has been explored using the large-scale bound constraint optimization tool (L-BFGS-B)[27] as a precursor to their use in fully coupled aero-structural optimization problems.

IV.D. Optimization to Achieve Prescribed Unsteady Beam Deflection

As a proof of concept we provide application of the developed methodology for a five-element beam model for an unsteady flap deflection problem. As an initial condition, the beam is given a small tip perturbation (using a tip load $F = 0.1N$) and then allowed to vibrate naturally. The objective is to optimize on the elemental design variables (such

as, $EI(i)\ i = [1 : nelem]$) so as to attain a *prescribed* flap deflection. To define the target tip flap deflection over a time period ($q_{tip_{ref}}(t)$), a linearly varying stiffness distribution is assigned ($EI \in [7500 : 12500] Nm^2$). Then the stiffness of the beam is initialized to $EI(i) = 10000$, $i = [1 : nelem]$ and the beam is optimized to obtain the target tip deflection (q_{ref}) variation over a time period. Design variables are defined as $x = EI(i), i = [1 : nelem]$, and the objective function for the unsteady problem as:

$$L_{obj} = ||q_{tip} - q_{tip_{ref}}||_2 + \beta \sum_{i}^{nelem} EI(i) \tag{31}$$

where the first term $f_1 = ||q_{tip} - q_{tip_{ref}}||_2$, refers to the second order norm of tip flap deflection over the whole time period considered (i.e. over 1.6 *revs* or $nstep = 1000$ time steps). The second term ($f_2 = \beta \sum_i^{nelem} EI(i), \beta = 10^{-9}$) refers to the weight penalty of the beam. The goal is : $min(L_{obj})$, subject to $l < x < u$; where l and u are the lower and upper bounds of design variables x (specifically EI values), taken as $l = 7500 Nm^2, u = 12500 Nm^2$.

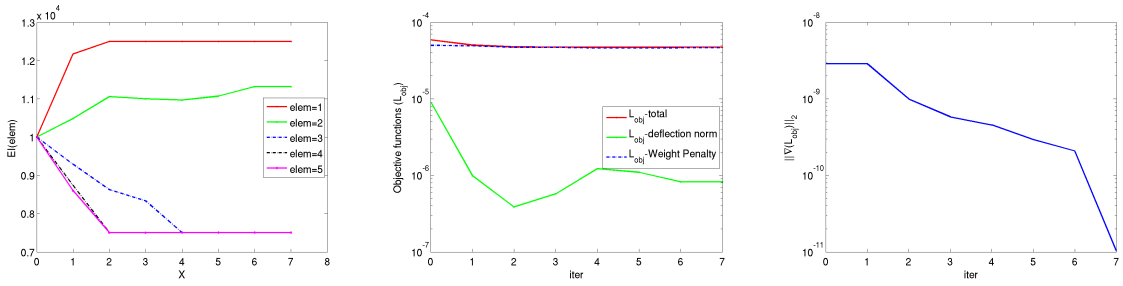

(a) Design variables x (EI) (b) Objective (c) Sensitivity

Figure 3. Convergence of EI distribution, L_{obj} and sensitivity for unsteady beam. (Red) $L_{obj}(= f_1 + f_2)$; (Green) f1; (Blue) f2

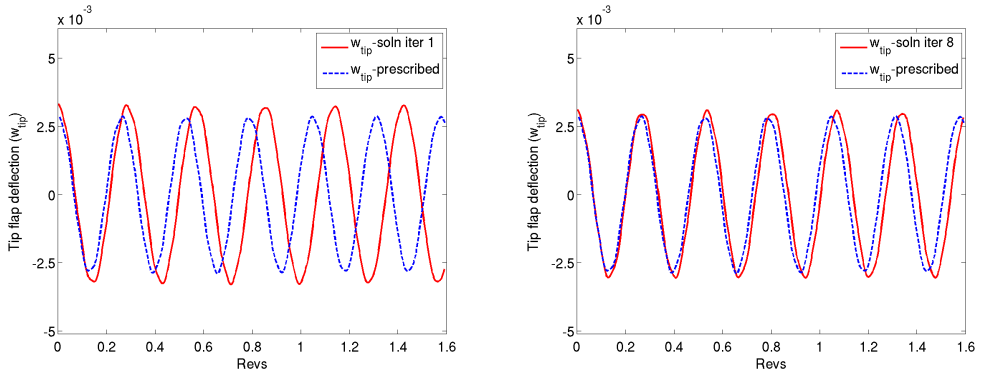

(a) iteration 1 (b) iteration 8

Figure 4. Flap deflection (w) convergence for unsteady beam (nelem=5)

Figure 3(a) show the evolution of stiffness distribution and Fig. 3(b) show the convergence of the objective function for the five element unsteady beam. The overall objective decreases only slightly over 8 design cycles due to the constraining effect of the penalty term. However the shape matching component f_1 of the objective decreases by several orders of magnitude, and the time history of the tip deflection closely matches the target at the final design cycle as shown in Figure 4. Additionally, Figure 3(c) shows that the sensitivity gradients are decreased by 2.5 orders of magnitude at the final design indicating that the process is converging towards an optimum.

V. Fully Coupled Fluid-Structure Analysis Formulation

V.A. Fluid-structure interface (FSI)

In addition to the solution of the aerodynamic problem and the structural dynamics problem, the solution of the fully coupled time-dependent aeroelastic problem requires the exchange of aerodynamic loads from the CFD solver to the beam structure, which in turn returns surface displacements to the fluid flow solver. The governing equations for the

FSI can be written in residual form as:

$$\mathbf{S}(\mathbf{F_b}, \mathbf{Q}, \mathbf{F}(\mathbf{x}, \mathbf{u})) = \mathbf{F_b} - [T(\mathbf{Q})]\mathbf{F}(\mathbf{x}, \mathbf{u}) = 0 \quad (32)$$

$$\mathbf{S}'(\mathbf{x_s}, \mathbf{Q}) = \mathbf{x_s} - [T(\mathbf{Q})]^T \mathbf{Q} = 0 \quad (33)$$

respectively for the forces transfered to the structural solver and displacements returned to the flow solver. In these equations, $[T]$ represents the transfer matrix which projects point-wise CFD surface forces $\mathbf{F}(\mathbf{x}, \mathbf{u})$ onto the individual beam elements resulting in the beam forces $\mathbf{F_b}$. The transpose of this matrix is used to obtain the CFD surface displacements $\mathbf{x_s}$ from the beam degrees of freedom $\mathbf{Q}$. Also note that $[T]$ is a function of $\mathbf{Q}$ since the transfer patterns change with the beam deflection.

V.B. General solution procedure

The aeroelastic problem consists of multiple coupled sets of equations namely, the mesh deformation equations, the flow equations (CFD), the beam model-based structural equations, and the fluid-structure interface transfer equations. The system of equations to be solved at each time step can be written as:

$$\mathbf{G}(\mathbf{x}, \mathbf{x_s}(\mathbf{Q})) = \mathbf{0} \quad (34)$$

$$\mathbf{R}(\mathbf{u}, \mathbf{x}) = \mathbf{0} \quad (35)$$

$$\mathbf{S}(\mathbf{F_B}, \mathbf{Q}, \mathbf{F}(\mathbf{x}, \mathbf{u})) = \mathbf{0} \quad (36)$$

$$\mathbf{J}(\mathbf{Q}, \mathbf{F_B}) = \mathbf{0} \quad (37)$$

$$\mathbf{S}'(\mathbf{x_s}, \mathbf{Q}) = \mathbf{0} \quad (38)$$

where $\mathbf{S}$ and $\mathbf{S}'$ represent the residuals of the FSI equations, and J represents the residual of the structural analysis problem. Note that the mesh motion residual now depends also on any surface deflections $\mathbf{x_s}$ introduced by the structural model.

Within each physical time step, solution of the fully coupled fluid structure problem consists of performing multiple coupling iterations on each discipline using the latest available values from the other disciplines. Thus the coupled iteration strategy proceeds as:

$$\left[\frac{\partial \mathbf{G}}{\partial \mathbf{x}}\right] \Delta \mathbf{x}^c = -\mathbf{G}(\mathbf{x^{c-1}}, \mathbf{x_s^{c-1}}) \quad (39)$$

$$\left[\frac{\partial \mathbf{R}}{\partial \mathbf{u}}\right] \Delta \mathbf{u}^c = -\mathbf{R}(\mathbf{u^{c-1}}, \mathbf{x^c}) \quad (40)$$

for the flow equations, where the superscript c denotes the coupling iteration index, and the variables are updated as $\mathbf{x^c} = \mathbf{x^{c-1}} + \Delta\mathbf{x^c}$ and $\mathbf{u^c} = \mathbf{u^{c-1}} + \Delta\mathbf{u^c}$. This is followed by the solution of the FSI and structural model as:

$$\mathbf{F_b^c} = [\mathbf{T}(\mathbf{Q^c})]\,\mathbf{F}(\mathbf{x^c}, \mathbf{u^c}) \quad (41)$$

$$\left[\frac{\partial \mathbf{J}}{\partial \mathbf{Q}}\right] \Delta \mathbf{Q}^c = -\mathbf{J}(\mathbf{Q^c}, \mathbf{F_b^c}) \quad (42)$$

$$\mathbf{x_s} = [T]^T \mathbf{Q}^c \quad (43)$$

In this implementation, subiterations are performed to converge the first two equations simultaneously for the final values of $\mathbf{Q^c}$, while the third equation corresponds to an explicit evaluation for the $\mathbf{x_s}$ given the $\mathbf{Q^c}$ values.

At the first coupling iteration, $\mathbf{x_s^c} = \mathbf{0}$ and solution of the mesh deformation equation is trivial, although non zero values of $\mathbf{x_s}$ are produced at subsequent coupling iterations as the beam deflects in response to the aero loads. From a disciplinary point of view, the aerodynamic solver produces updated values of $\mathbf{u}$ and $\mathbf{x}$, which are used to compute $\mathbf{F}(\mathbf{x}, \mathbf{u})$ pointwise surface forces. These surface forces are input to the FSI/structural model which returns surface displacements $\mathbf{x_s}$. These new surface displacements are then fed back into the mesh deformation equations and the entire procedure is repeated until convergence is obtained for the full coupled aero-structural problem at the given time step.

VI. Sensitivity Analysis for Coupled Aeroelastic Problem

In the formulation of the sensitivity analysis for the coupled aeroelastic problem, it is desirable to mimic as closely as possible the solution strategies and data structures employed for the analysis problem. Thus, analogous disciplinary

solvers can be reused for each disciplinary sensitivity problem, and the analysis coupling strategy can be extended to the sensitivity analysis formulation. Furthermore, the data transfered between disciplinary solvers should consist of vectors of the same dimension for the analysis, tangent and adjoint formulations. Starting with the forward sensitivity problem, the sensitivity of an objective L can be written as:

$$\frac{dL}{d\mathbf{D}} = \begin{bmatrix} \frac{\partial L}{\partial \mathbf{x}} & \frac{\partial L}{\partial \mathbf{u}} \end{bmatrix} \begin{bmatrix} \frac{\partial \mathbf{x}}{\partial \mathbf{D}} \\ \frac{\partial \mathbf{u}}{\partial \mathbf{D}} \end{bmatrix} \tag{44}$$

where the individual disciplinary sensitivities are given as the solution of the coupled system:

$$\begin{bmatrix} \frac{\partial \mathbf{G}}{\partial \mathbf{x}} & 0 & 0 & 0 & 0 & \frac{\partial \mathbf{G}}{\partial \mathbf{x_s}} \\ \frac{\partial \mathbf{R}}{\partial \mathbf{x}} & \frac{\partial \mathbf{R}}{\partial \mathbf{u}} & 0 & 0 & 0 & 0 \\ -\frac{\partial \mathbf{F}}{\partial \mathbf{x}} & -\frac{\partial \mathbf{F}}{\partial \mathbf{u}} & I & 0 & 0 & 0 \\ 0 & 0 & \frac{\partial \mathbf{S}}{\partial \mathbf{F}} & \frac{\partial \mathbf{S}}{\partial \mathbf{F_b}} & \frac{\partial \mathbf{S}}{\partial \mathbf{Q}} & 0 \\ 0 & 0 & 0 & \frac{\partial \mathbf{J}}{\partial \mathbf{F_b}} & \frac{\partial \mathbf{J}}{\partial \mathbf{Q}} & 0 \\ 0 & 0 & 0 & 0 & \frac{\partial \mathbf{S}'}{\partial \mathbf{Q}} & \frac{\partial \mathbf{S}'}{\partial \mathbf{x_s}} \end{bmatrix} \begin{bmatrix} \frac{\partial \mathbf{x}}{\partial \mathbf{D}} \\ \frac{\partial \mathbf{u}}{\partial \mathbf{D}} \\ \frac{\partial \mathbf{F}}{\partial \mathbf{D}} \\ \frac{\partial \mathbf{F_b}}{\partial \mathbf{D}} \\ \frac{\partial \mathbf{Q}}{\partial \mathbf{D}} \\ \frac{\partial \mathbf{x_s}}{\partial \mathbf{D}} \end{bmatrix} = \begin{bmatrix} -\frac{\partial \mathbf{G}}{\partial \mathbf{D}} \\ 0 \\ 0 \\ 0 \\ 0 \\ 0 \end{bmatrix}$$

The first and second equations correspond to equations for the mesh and flow variable sensitivities, as previously described for the aerodynamic solver, and the third equation corresponds to the construction of the surface force sensitivities given these two previous sensitivities. The fourth equation denotes the sensitivity of the FSI transfer from the fluid to the structural solver, while the fifth equation corresponds to the sensitivity of the structural solver. Finally, the last equation corresponds to the sensitivity of the FSI transfer from the structural solver back to the flow solver. This coupled system of sensitivities can be solved analogously to the coupled analysis problem as:

$$\left[\frac{\partial \mathbf{G}}{\partial \mathbf{x}}\right] \frac{\partial \mathbf{x}}{\partial \mathbf{D}}^{c} = -\frac{\partial \mathbf{G}}{\partial \mathbf{x_s}} \frac{\partial \mathbf{x}}{\partial \mathbf{D}}^{\mathbf{c-1}} - \frac{\partial \mathbf{G}}{\partial \mathbf{D}} \tag{45}$$

$$\left[\frac{\partial \mathbf{R}}{\partial \mathbf{u}}\right] \frac{\partial \mathbf{u}}{\partial \mathbf{D}}^{\mathbf{c}} = -\frac{\partial \mathbf{R}}{\partial \mathbf{x}} \frac{\partial \mathbf{x}}{\partial \mathbf{D}}^{\mathbf{c}} \tag{46}$$

followed by the explicit evaluation of the surface force sensitivities as:

$$\frac{\partial \mathbf{F}}{\partial \mathbf{D}}^{\mathbf{c}} = \frac{\partial \mathbf{F}}{\partial \mathbf{x}} \frac{\partial \mathbf{x}}{\partial \mathbf{D}}^{\mathbf{c}} + \frac{\partial \mathbf{F}}{\partial \mathbf{u}} \frac{\partial \mathbf{u}}{\partial \mathbf{D}}^{\mathbf{c}} \tag{47}$$

These sensitivity evaluations are all implemented within the flow solver. They are followed by the solution of the remaining components of the system as:

$$\begin{bmatrix} \frac{\partial \mathbf{S}}{\partial \mathbf{F_b}} & \frac{\partial \mathbf{S}}{\partial \mathbf{Q}} \\ \frac{\partial \mathbf{J}}{\partial \mathbf{F_b}} & \frac{\partial \mathbf{J}}{\partial \mathbf{Q}} \end{bmatrix} \begin{bmatrix} \frac{\partial \mathbf{F_b}}{\partial \mathbf{D}}^{c} \\ \frac{\partial \mathbf{Q}}{\partial \mathbf{D}}^{c} \end{bmatrix} = \begin{bmatrix} -\frac{\partial \mathbf{S}}{\partial \mathbf{F}} \frac{\partial \mathbf{F}}{\partial \mathbf{D}}^{c} \\ 0 \end{bmatrix} \tag{48}$$

These two equations are solved simultaneously to obtain the structural sensitivities $\frac{\partial \mathbf{Q}}{\partial \mathbf{D}}$ which are then used to evaluate the surface mesh sensitivities explicitly as:

$$\frac{\partial \mathbf{x_s}}{\partial \mathbf{D}}^c = -\frac{\partial \mathbf{S}'}{\partial \mathbf{Q}} \frac{\partial \mathbf{Q}}{\partial \mathbf{D}}^c \tag{49}$$

where the fact that $\frac{\partial \mathbf{S}'}{\partial \mathbf{x_s}} = [I]$ (identity matrix) has been used. These new surface mesh sensitivities are then fed back into the first equation in the system initiating the next coupling iteration. As can be seen, each disciplinary solution procedure requires the inversion of the same Jacobian matrix as the corresponding analysis problem, which is done using the same iterative solver. Furthermore, the fluid-structure coupling requires the transfer of the force sensitivities $\frac{\partial \mathbf{F}}{\partial \mathbf{D}}$ from the flow to the structural solver, and the surface mesh sensitivities $\frac{\partial \mathbf{x_s}}{\partial \mathbf{D}}$ from the structural solver back to the fluid solver, which are of the same dimension as the force and surface displacements transfered in the analysis problem, respectively.

The corresponding adjoint problem can be obtained by premultiplying equation (45) by the inverse of the large coupling matrix and substituting this into equation (44), transposing the entire system, and defining adjoint variables as solutions to the following coupled system:

$$\begin{bmatrix} \frac{\partial \mathbf{G}}{\partial \mathbf{x}}^T & \frac{\partial \mathbf{R}}{\partial \mathbf{x}}^T & -\frac{\partial \mathbf{F}}{\partial \mathbf{x}}^T & 0 & 0 & 0 \\ 0 & \frac{\partial \mathbf{R}}{\partial \mathbf{u}}^T & -\frac{\partial \mathbf{F}}{\partial \mathbf{u}}^T & 0 & 0 & 0 \\ 0 & 0 & I & \frac{\partial \mathbf{S}}{\partial \mathbf{F}}^T & 0 & 0 \\ 0 & 0 & 0 & \frac{\partial \mathbf{S}}{\partial \mathbf{F_b}}^T & \frac{\partial \mathbf{J}}{\partial \mathbf{F_b}}^T & 0 \\ 0 & 0 & 0 & \frac{\partial \mathbf{S}}{\partial \mathbf{Q}}^T & \frac{\partial \mathbf{J}}{\partial \mathbf{Q}}^T & \frac{\partial \mathbf{S}'}{\partial \mathbf{Q}}^T \\ \frac{\partial \mathbf{G}}{\partial \mathbf{x_s}}^T & 0 & 0 & 0 & 0 & \frac{\partial \mathbf{S}'}{\partial \mathbf{x_s}}^T \end{bmatrix} \begin{bmatrix} \Lambda_{\mathbf{x}} \\ \Lambda_{\mathbf{u}} \\ \Lambda_{\mathbf{F}} \\ \Lambda_{\mathbf{F_b}} \\ \Lambda_{\mathbf{Q}} \\ \Lambda_{\mathbf{x_s}} \end{bmatrix} = \begin{bmatrix} \frac{\partial \mathbf{L}}{\partial \mathbf{x}}^T \\ \frac{\partial \mathbf{L}}{\partial \mathbf{u}}^T \\ 0 \\ 0 \\ 0 \\ 0 \end{bmatrix}$$

This system can be solved starting with the last equation and proceeding to the first equation as:

$$\Lambda_{\mathbf{x_s}}{}^c = -\frac{\partial \mathbf{G}}{\partial \mathbf{x_s}}^T \Lambda_{\mathbf{x}}{}^{c-1} \tag{50}$$

followed by the solution of the structural adjoints

$$\begin{bmatrix} \frac{\partial \mathbf{S}}{\partial \mathbf{F_b}}^T & \frac{\partial \mathbf{J}}{\partial \mathbf{F_b}}^T \\ \frac{\partial \mathbf{S}}{\partial \mathbf{Q}}^T & \frac{\partial \mathbf{J}}{\partial \mathbf{Q}}^T \end{bmatrix} \begin{bmatrix} \Lambda_{\mathbf{F_b}}{}^c \\ \Lambda_{\mathbf{Q}}{}^c \end{bmatrix} = \begin{bmatrix} 0 \\ -\frac{\partial \mathbf{S}'}{\partial \mathbf{Q}}^T \Lambda_{\mathbf{x_s}}{}^c \end{bmatrix} \tag{51}$$

followed by the explicit construction of the pointwise CFD surface force adjoint:

$$\Lambda_{\mathbf{F}}{}^c = -\frac{\partial \mathbf{S}}{\partial \mathbf{F}}^T \Lambda_{\mathbf{F_b}}{}^c \tag{52}$$

and ending with the solution of the mesh and flow adjoints as:

$$\begin{bmatrix} \frac{\partial \mathbf{G}}{\partial \mathbf{x}^T} & \frac{\partial \mathbf{R}}{\partial \mathbf{x}^T} \\ 0 & \frac{\partial \mathbf{R}}{\partial \mathbf{u}^T} \end{bmatrix} \begin{bmatrix} \Lambda_{\mathbf{x}}{}^c \\ \Lambda_{\mathbf{u}}{}^c \end{bmatrix} = \begin{bmatrix} \frac{\partial L}{\partial \mathbf{x}}^T + \frac{\partial \mathbf{F}}{\partial \mathbf{x}}^T \Lambda_{\mathbf{F}}{}^c \\ \frac{\partial L}{\partial \mathbf{u}}^T + \frac{\partial \mathbf{F}}{\partial \mathbf{u}}^T \Lambda_{\mathbf{F}}{}^c \end{bmatrix} \tag{53}$$

Once again, the solution of the various disciplinary adjoints requires the inversion of the corresponding disciplinary Jacobians (transposed in this case) which can be accomplished using the same iterative solvers as for the analysis and forward sensitivity problems. Additionally, the input to the structural adjoint problem consists of the variable $\Lambda_{\mathbf{x_s}}$, which is the same dimension as the surface displacements output from the structural analysis solver, while the output of the structural adjoint solver consists of the variable $\Lambda_{\mathbf{F}}$ which is of the same dimension as the force inputs to the structural solver in the analysis problem.

VII. Verification of Coupled Aeroelastic Sensitivity

The forward and adjoint sensitivities for the coupled aeroelastic problem are verified using the complex step method. Any function $f(x)$ operating on a real variable x can be utilized to compute the derivative $f'(x)$ by redefining the input variable x and all intermediate variables used in the discrete evaluation of $f(x)$ as complex variables. For a complex input, the function when redefined as described produces a complex output. The derivative of the real function $f(x)$ can be computed by expanding the complex operator $f(x+ih)$ as:

$$f(x+ih) = f(x) + ihf'(x) + \cdots \tag{54}$$

from which the derivative $f'(x)$ can be easily determined as:

$$f'(x) = \frac{Im\left[f\left(x+ih\right)\right]}{h} \tag{55}$$

As in the case of finite-differencing, the complex step-based differentiation also requires a step size. However, unlike finite-differencing the complex step method is insensitive to small step sizes since no differencing is required. In theory it is possible to verify forward and adjoint-based gradients using the complex step method to machine precision. With this in mind, a complex version of the complete coupled aero-structural analysis code has been constructed through scripting of the original source code to redefine variables from real to complex types and to overload a small number of functions for use with complex variables.

VII.A. Unsteady Test Problem

The Hart2 rotor in hover is solved both for a rigid blade (no structural model) as well as for a flexible blade (coupled with structure). For the latter, the flow is solved in tight coupling with the beam solver. The mixed element mesh made up of prizms, pyramids and tetrahedra consists of approximately 2.32 million grid points and is shown in Figures (5(a)), (5(b)) and (5(c)), where the rigid blade simulation is compared with the coupled CFD/CSD simulation. The simulations are run for three rotor revolutions using a 2 degree time-step for 540 time-steps starting from freestream initialization. For the rigid blade simulation, the time-dependent mesh motion is determined by rotating the entire mesh as a solid body at each time step. The unsteady Reynolds-averaged Navier-Stokes equations are solved at each time step in ALE form, using the Spalart-Allmaras turbulence model. Figures (6(a)) and (6(b)) shows a snapshot of the pressure coefficient contours on the rotor at the end of a single revolution for both the rigid and flexible blades.

The coupled CFD/CSD simulation is run in a similar manner. However, the flow solution (CFD) is coupled with the beam solver (CSD) every time step by appropriately exchanging, a) airloads information from the flow domain to the beam and b) blade deformation information from the beam to the flow domain, at the fluid-structure interface (i.e. blade surface). In this coupled simulation, the mesh is first moved according the deformations dictated by the new flexed blade coordinates determined from the structural beam code before the solid body rotation of the entire mesh is performed. Thus, the flow now sees not only the rigidly rotated mesh (observed in rigid blade simulation), but also the deformed mesh around the blades. This coupled fluid-structure interaction problem needs to be iterated until satisfactory convergence is achieved on both flow and mesh deformation within each time step. This kind of CFD/CSD coupling done within every time step is known as *tight coupling*.

The simulations were performed on the Yellowstone supercomputer at the NCAR-Wyoming Supercomputing Center (NWSC), with the analysis problem running in parallel on 512 cores. Each time step used 6 coupling iterations, and each coupling iteration used 10 non-linear flow iterations with each non-linear iteration consisting of a three-level line-implicit multigrid cycle. The typical simulation for 3 rotor revolutions required around 3 hours of total run time.

Figures 7 through 10 summarize the overall convergence of the rigid and aero-elastic coupling analysis formulations. Figure 7 shows the typical flow and turbulence residual convergence within a single time step for the rigid rotor case (no structural model), while Figure 8 depicts convergence of the flow and turbulence residuals at the same time step for the coupled aeroelastic case. In this case, the jumps in residual values at the start of new coupling iterations

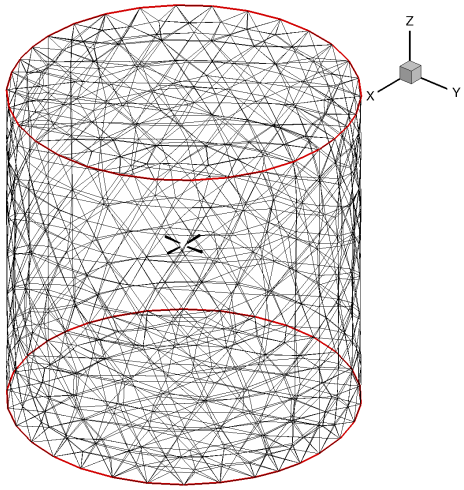

(a) Computational Domain

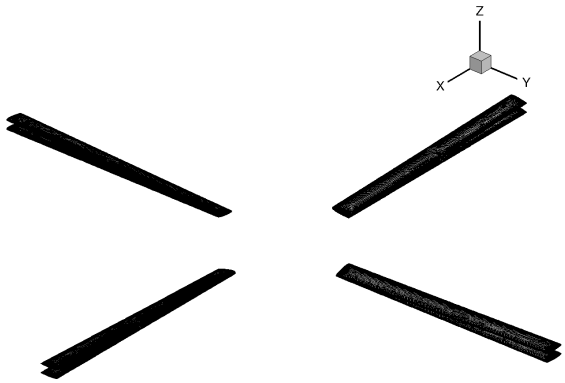

(b) Planform view

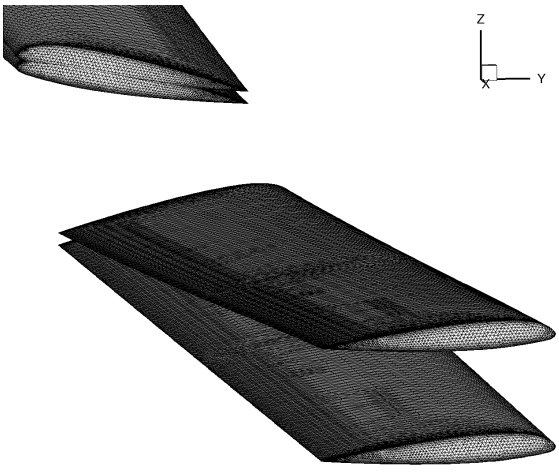

(c) Zoomed in view

Figure 5. HART2 rotor mesh consisting of 2.32 million points used in the optimization example.

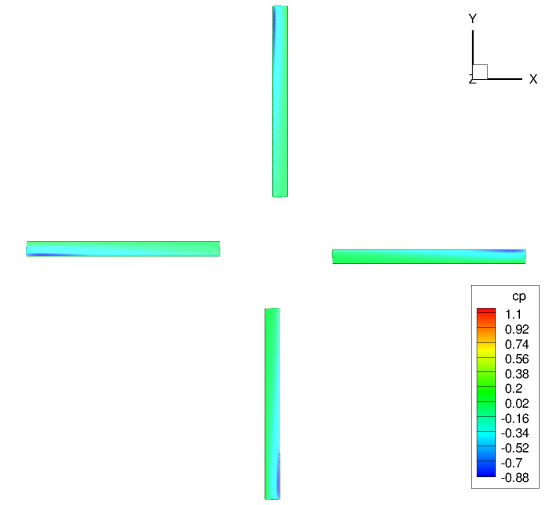

(a) Planform view

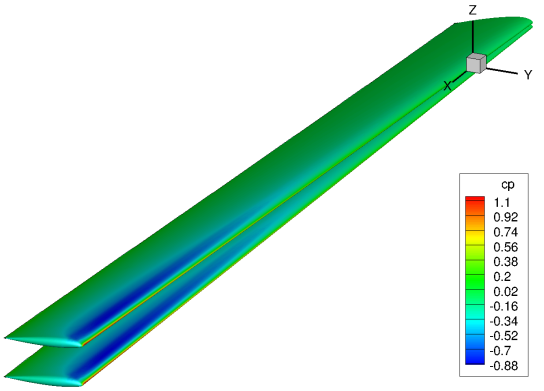

(b) Zoomed in view

Figure 6. C_P **contours for the baseline HART2 rotor, with flexible and rigid blades, in hover after one revolution. The mesh consists of 2.32 million vertices.**

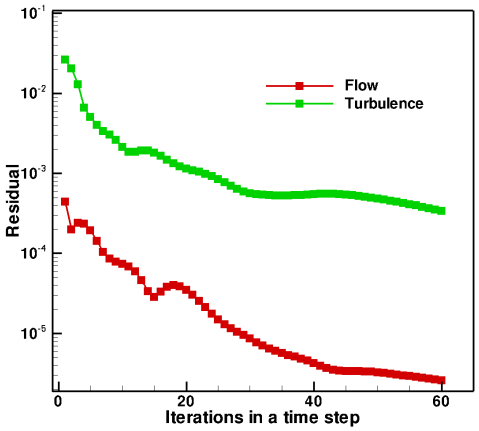

Figure 7. Flow and turbulence residual convergence at a given time step for rigid analysis

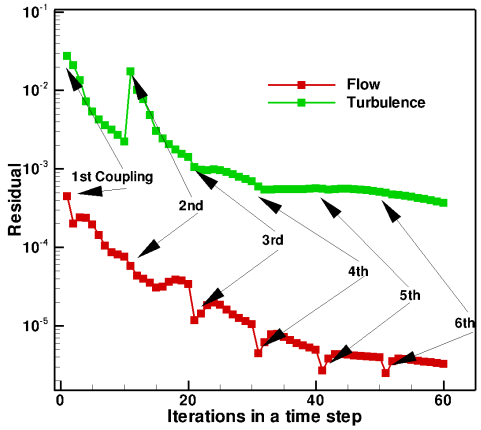

Figure 8. Flow and turbulence residual convergence at a given time step for coupled aeroelastic analysis

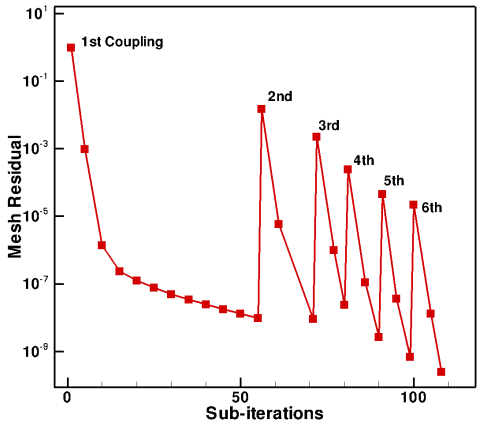

Figure 9. Mesh deformation residual convergence at a given time step for coupled aeroelastic analysis

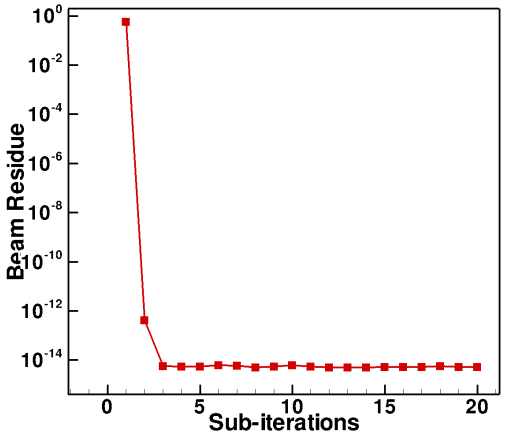

Figure 10. Residual convergence of beam and overall FSI in one coupling iteration

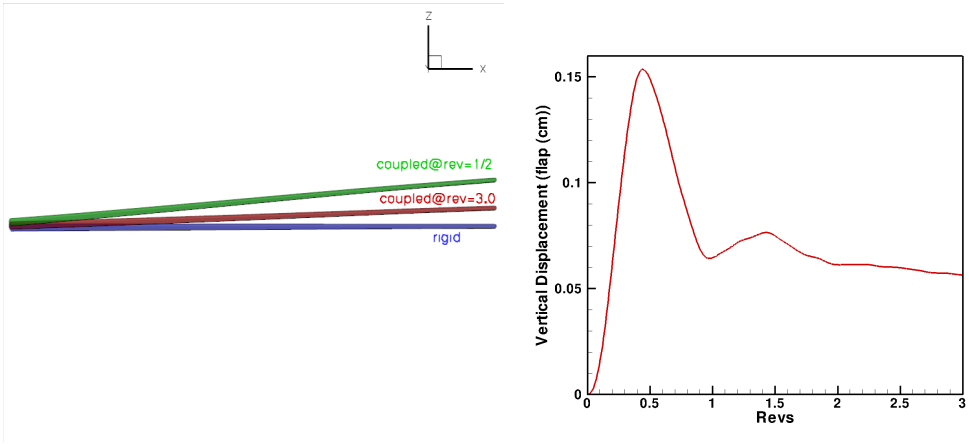

(a) Blade Deformation (b) Blade tip vs time

Figure 11. HART2 blade deformation

are clearly visible, although these jumps become smaller as the coupling procedure converges, and the overall residual histories closely follow those of the rigid rotor case after the first few coupling iterations. (The drop in density residual at each new coupling iteration is due to the imposition of a small start-up CFL value at each new coupling iteration.) Figure 9 depicts the convergence of the mesh deformation residual for the same time step, also showing jumps in the residual at the start of each new coupling iteration. Solution of the mesh deformation equations terminates when the residuals reach a prescribed tolerance of 1.e-08, thus the variable number of iterations per coupling cycle. Most notable is the fact that the initial mesh deformation residual decreases at each new coupling iteration, providing a measure of the convergence of the entire coupling procedure. Figure 10 illustrates the convergence of the coupled beam/FSI residual (i.e. equations (36) and (37)), showing rapid convergence to machine zero in a small number of iterations within a single CFD/CSD coupling iteration. The corresponding beam residual drop is observed to be of 15 orders of magnitude, as shown in Fig. 10. The effect of the CFD/CSD aeroelastic coupling is clearly demonstrated in Figure 11, which compares the deformed blade shape from the coupled simulation with that from the rigid blade simulation. As Figure 11(b) shows, the blade initially deforms onto larger tip flap values ($\sim 16cm$) before settling into a lower value of $\sim 6cm$. Further Figure 12 compares thrust and torque values from the coupled solution with the rigid blade solution. The flexed blade results in prediction of more coning of the blade and slightly lower total thrust (Fig. 12(a)) as well as lower total torque magnitude (Fig. 12(b)). Therefore, it is evident that the rigid body model might lead to over prediction of required rotor torque.

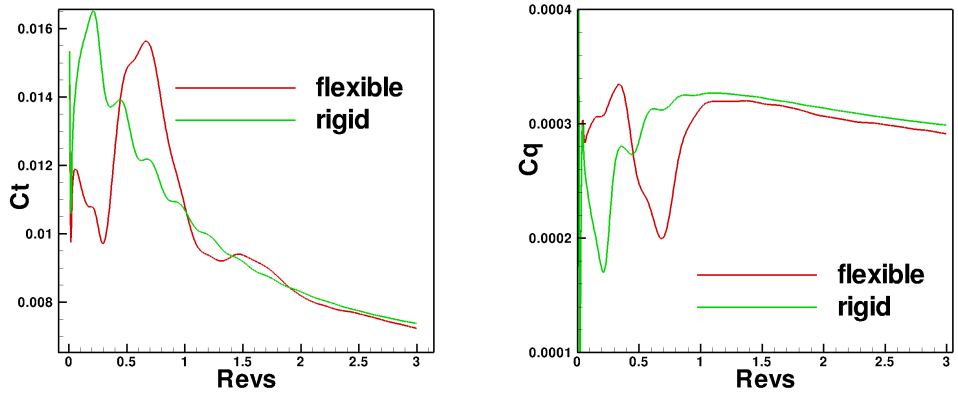

(a) Thrust vs time (b) Torque vs time

Figure 12. Time history of airloads on HART2 rotor

VII.B. Geometry Parameterization

In order to obtain sensitivities with respect to a set of shape parameters that are well suited for design optimization purposes, a baseline blade is constructed by stacking 11 airfoil section along the span. Each airfoil contains 10 Hicks-Henne bump functions 5 on the upper surface and 5 on the lower surface that can be used to modify the airfoil shape. Additionally, the twist values of the blade at the root and tip airfoil sections are also used as design variables resulting in a total of 112 design variables. Figure (13(a)) provides an illustration of the baseline blade design setup. A high density structured mesh is generated about this blade geometry, which is then rotated and translated to match each individual blade in the CFD mesh, as shown in Figure (13(b)). Interpolation patterns between each unstructured mesh surface point and the baseline structured mesh are determined in a preprocessing phase. These interpolation patterns are then used to interpolate shape changes from the baseline blade to all four blades in the CFD mesh (as determined by changes in the design variables) and to transfer sensitivities from the surface CFD mesh points to the design variables using the chain rule of differentiation.

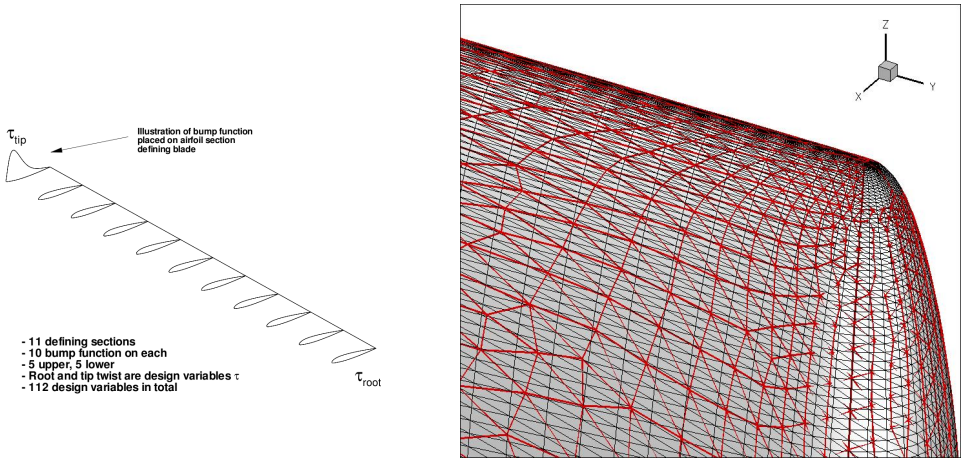

(a) Blade design parameters (b) Baseline structured blade mesh overlap with CFD mesh

Figure 13. Illustration of (a) baseline blade with design parameters and (b) overlap in tip region between baseline blade structured mesh and CFD surface unstructured mesh.

VII.C. Unsteady Objective Function Formulation

A time-integrated objective function based on the time variation of the thrust (C_T) and torque (C_Q) coefficients is used for this test case. The goal of the optimization is to reduce the time-integrated torque coefficient while constraining the time-integrated thrust coefficient to the baseline rotor performance. The objective function is based on the summation of the differences between a target and a computed objective value at each time level n . Mathematically the local objective function at each time-step in the integration range is defined as:

$$L^n = (\delta C_T^n)^2 + 10(\delta C_Q^n)^2 \tag{56}$$

$$\delta C_T^n = (C_T^n - C_{T\,target}^n) \tag{57}$$

$$\delta C_Q^n = (C_Q^n - C_{Q\,target}^n) \tag{58}$$

where the target thrust coefficient values at each time-step in the integration range are set from the baseline HART2 rotor values and the target torque values are set to zero. The weight of 10 on the torque coefficient is necessary to equalize the difference in orders-of-magnitude between the thrust and torque coefficients. The global or time-integrated objective is then constructed using equal unit weights at each time-step as:

$$L^g = \sum_{n=1}^{n=N} L^n \tag{59}$$

VIII. Fully Coupled CFD/CSD Adjoint: Unsteady Sensitivity Verification

The fully coupled CFD/CSD adjoint formulation was verified by first comparing the tangent sensitivities with those obtained from complex step method. Further the adjoint formulation was verified by comparing its sensitivities with those obtained from the tangent as well as the complex step method.

VIII.A. Forward Sensitivity Verification

The tangent formulation was verified for perturbations on one geometric design parameter, namely, blade twist at the tip, for both uncoupled (rigid blade) as well as coupled simulations. As described earlier, a complex perturbation of size 1×10^{-100} is introduced on twist at the beginning of the analysis run. The derivatives of the functional (L^n) are evaluated and compared with those obtained using the forward linearization procedure at every time instance for up to 5 time steps. In both cases, for the complex step method, as well as for the forward linearization approach, the fully coupled aeroelastic problem is converged to machine zero at each time step in order to avoid contaminating the sensitivity values with errors due to incomplete convergence.

Tables (2) and (3), respectively, compare rigid aerodynamic only derivatives and coupled aeroelastic derivatives ($\frac{\partial L^n}{\partial D}$) obtained from the complex analysis run with those from the forward linearization run for the first 5 time steps. The uncoupled tangent verification serves as a sanity check of the new forward sensitivity formulation when the structural code is switched off. As can be seen from the tables, the forward tangent sensitivities and the complex step sensitivities agree to 12 significant digits for both the rigid and flexible aeroelastic rotor cases.

Table 2. Uncoupled forward linearization verification

n[a]	**Method**	**Uncoupled (Rigid)**
1	Complex	4.096552182858**29**E-006
	Tangent	4.096552182858**30**E-006
2	Complex	6.149890891151**60**E-006
	Tangent	6.149890891151**50**E-006
3	Complex	7.459751648971**305**E-006
	Tangent	7.459751648971**288**E-006
4	Complex	8.387775876237**77**E-006
	Tangent	8.387775876237**60**E-006
5	Complex	9.168900547740**15**E-006
	Tangent	9.168900547740**23**E-006

[a]n=number of time step

VIII.B. Adjoint Sensitivity Verification

Having validated the forward sensitivity with that from the complex step method, the adjoint formulation was validated with these two formulations. Table 3 compares the three formulations for 5 unsteady time steps as before. The sensitivity values from the adjoint formulation matches to twelve significant digits with the other two formulations. This provides the confidence in the present methodology to be used as an effective aeroelastic optimization tool.

IX. Helicopter Blade Optimization

The same Hart2 rotor blade considered for analysis is used for the optimization test problem. The solution methodology is similar to what was described for the analysis problem. However, for the optimization problem the simulation was performed for only one and a half rotor revolutions, using a 2° time step size. The optimization procedure used

Table 3. Coupled adjoint linearization verification

n	Method(n)	Coupled (Aeroelastic)
1	Complex	3.690007037237**534**E-006
	Tangent	3.690007037237**471**E-006
	Adjoint	3.690007037237**598**E-006
2	Complex	5.150483530831**191**E-006
	Tangent	5.150483530831**145**E-006
	Adjoint	5.150483530831**289**E-006
3	Complex	5.828069793498**591**E-006
	Tangent	5.828069793498**538**E-006
	Adjoint	5.828069793498**741**E-006
4	Complex	6.056211086344**925**E-006
	Tangent	6.056211086344**902**E-006
	Adjoint	6.056211086345**518**E-006
5	Complex	6.026286742020**757**E-006
	Tangent	6.026286742020**644**E-006
	Adjoint	6.026286742020**636**E-006

is the L-BFGS-B bounded reduced Hessian algorithm.[27] Each request by the optimization driver for a function and gradient value results in a single forward time-integration of the analysis solver and a single backward integration in time of the adjoint solver. A bound of $\pm 2\%$ chord for each defining airfoil section was set on the Hicks-Henne bump functions, and a bound of $\pm 0.5^\circ$ of twist was set on the root and tip twist definitions. The optimization was performed on the Yellowstone supercomputer at the NCAR-Wyoming Supercomputing Center (NWSC) with the simulations (analysis/adjoint) running in parallel on 1024 cores. Each time step in the analysis problem employed 6 coupling cycles. Each coupling cycle used 10 nonlinear iterations with each nonlinear iteration requiring 3 linear multigrid cycles per Krylov vector. The time required for a single function/gradient call was approximately 1.4 hours of wall clock time. The optimization problem was run for 4 design cycles which had 5 function calls in total.

Figures 14 shows the residual convergence for a typical unsteady adjoint time step. The figure shows the residual drops by 5 orders of magnitude over 6 coupling cycles. Figures 15(a) and 15(b) show the functional and gradient convergence over 4 design cycles. The figures show that, the functional is already dropping while the gradient value is being reduced.

Figures 16 compare the optimized Hart2 rotor load time history with that from the baseline rotor. The optimized rotor results in almost same thrust values as the baseline rotor with only 1% reduction in thrust (Fig. 16(a)) and achieves a 2% reduction in torque (Fig. 16(b)). Figure 17 further compares the optimized rotor blade tip time history with the baseline rotor and shows that the optimized rotor results in a rotor blade with reduced bending. Finally, Figures 18 compare the optimized rotor blade sections with the baseline sections. As the figure shows, the root stations are modified more than the tip stations.

X. Conclusions and Future Works

In this work, a discrete adjoint formulation for time-dependent tightly coupled aeroelastic three-dimensional problems has been developed and demonstrated. The formulation is designed to reuse as much as possible the original coupled aeroelastic data-structures and solution strategies used for the analysis problem, thus simplifying implementation and verification. A comprehensive verification approach was used to determine the accuracy of the adjoint sensitivities. In a first step, the individual disciplinary components of the adjoint sensitivity analysis formulation were verified independently using the forward tangent and complex step method. In a second step, these individual components were linked together and verification of the fully coupled aeroelastic sensitivities was demonstrated to machine precision. The adjoint sensitivities were used to perform a shape optimization problem for a flexible time-dependent rotor problem. The optimization problem used a relatively coarse mesh and was run for only several design iterations due to resource limitations. Future work will concentrate on demonstrating the potential of this approach for aeroelastic design optimization problems involving a larger number of design iterations, using finer meshes and smaller time

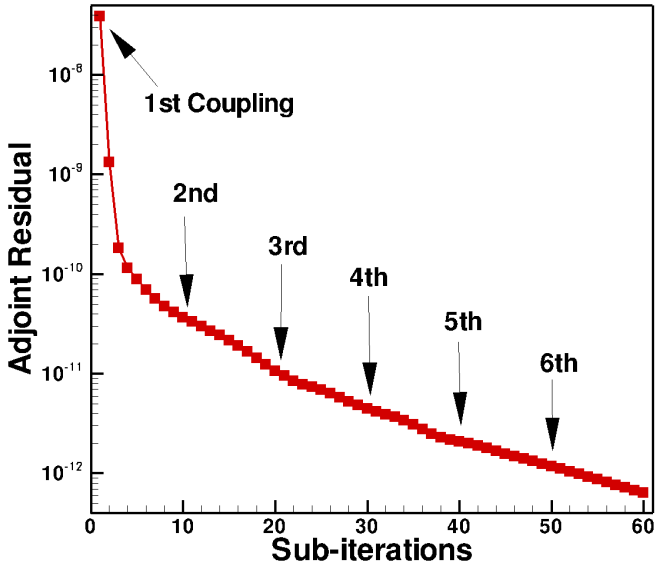

Figure 14. Residue convergence in a typical adjoint time step

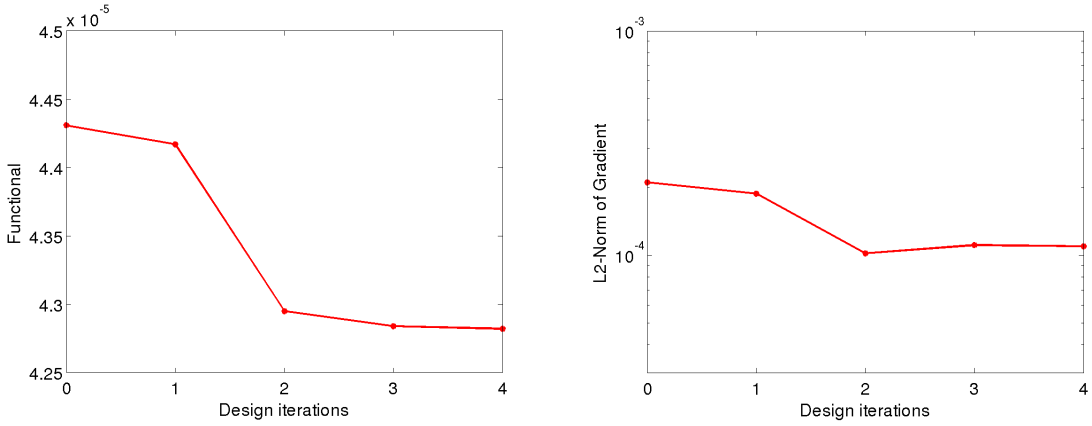

(a) Functional Convergence

(b) Gradient Convergence

Figure 15. Convergence in design optimization

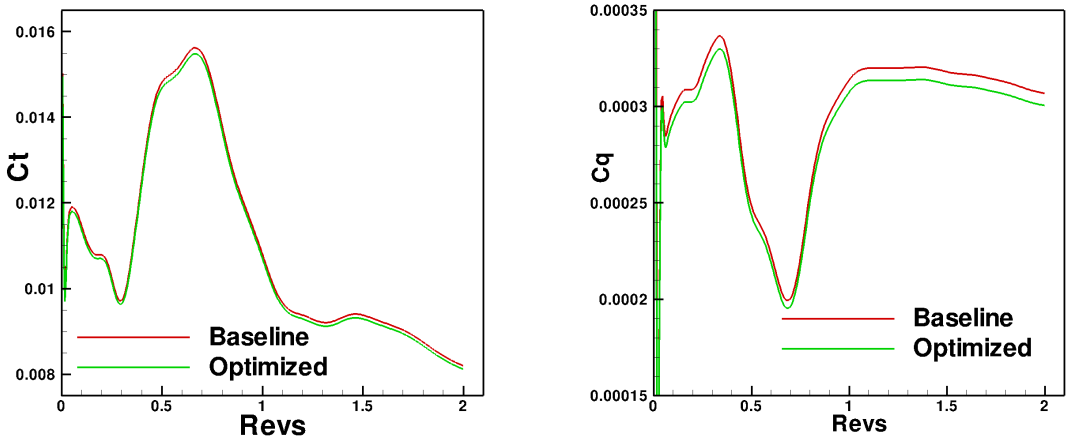

(a) Thrust vs time

(b) Torque vs time

Figure 16. Time history of airloads on optimized and baseline HART2 rotor

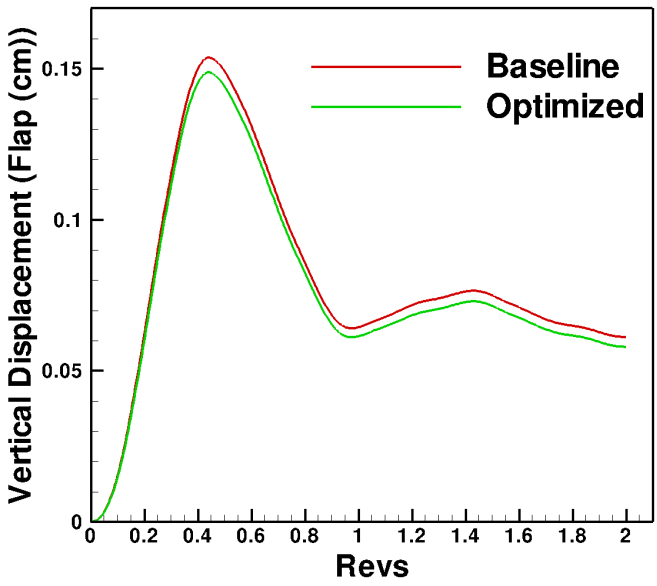

Figure 17. Optimized and baseline Hart2 rotor blade tip time history

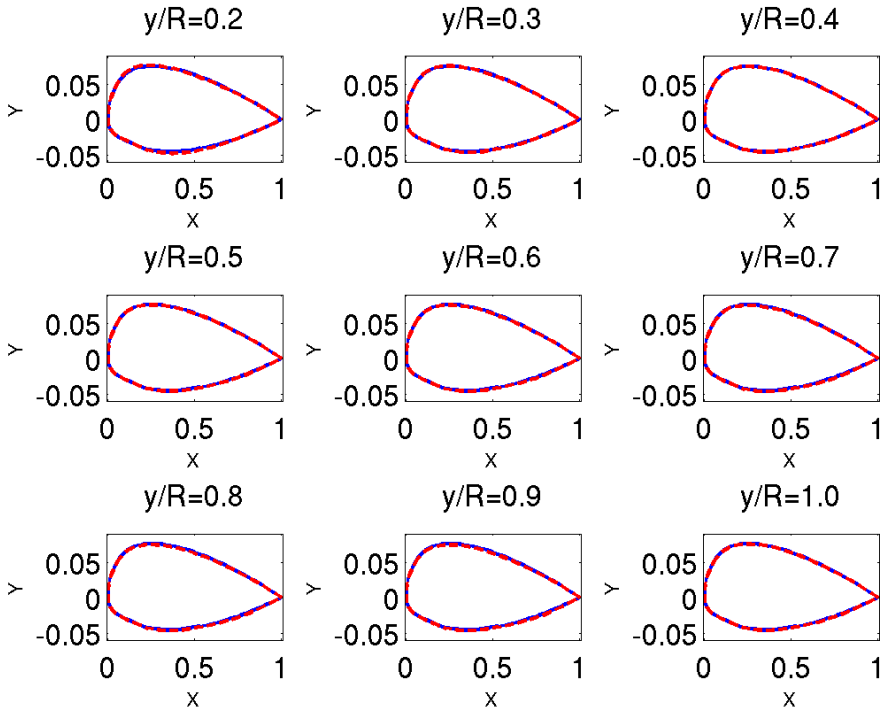

Figure 18. Optimized (red dashes) and baseline (blue solid) Hart2 rotor blade sections ($y/R = [0.2 : 1.0]$)

steps. More realistic design scenarios, including multiple constraints and multi-point optimization problems will also be considered.

XI. Acknowledgements

This work was partly funded by the Alfred Gessow Rotorcraft Center of Excellence through a subcontract with the University of Maryland. Partial support was also provided by AFOSR STTR Phase 1 contract FA9550-12C-0048. Computer resources were provided by the University of Wyoming Advanced Research Computing Center and by the NCAR-Wyoming Supercomputer Center.

References

[1]Jameson, A., "Aerodynamic Shape Optimization using the Adjoint Method," VKI Lecture Series on Aerodynamic Drag Prediction and Reduction, von Karman Institute of Fluid Dynamics, Rhode St Genese, Belgium, 2003.

[2]Jameson, A. and Vassberg, J., "Computational Fluid Dynamics for Aerodynamic Design: Its Current and Future Impact," Proceedings of the 39th Aerospace Sciences Meeting and Exhibit, Reno NV, AIAA Paper 2001–0538, 2001.

[3]Nadarajah, S. and Jameson, A., "A Comparison of the Continuous and Discrete Adjoint Approach to Automatic Aerodynamic Optimization," Proceedings of the 38th Aerospace Sciences Meeting and Exhibit, Reno NV, AIAA Paper 2000–0667, 2000.

[4]Nielsen, E. and Anderson, W., "Recent Improvements in Aerodynamic Design Optimization on Unstructured Meshes," *AIAA Journal*, Vol. 40-6, June 2002, pp. 1155–1163.

[5]Jameson, A., Alonso, J., Reuther, J., Martinelli, L., and Vassberg, J., "Aerodynamic shape optimization techniques based on control theory," AIAA Paper 98–2538, 1998.

[6]Giles, M., Duta, M., and Muller, J., "Adjoint Code Developments Using Exact Discrete Approach," AIAA Paper 2001–2596, 2001.

[7]Mani, K. and Mavriplis, D. J., "Unsteady Discrete Adjoint Formulation for Two-Dimensional Flow Problems with Deforming Meshes," *AIAA Journal*, Vol. 46-6, June 2008, pp. 1351–1364.

[8]Rumpfkeil, M. and Zingg, D., "A General Framework for the Optimal Control of Unsteady Flows with Applications," 45th AIAA Aerospace Sciences Meeting and Exhibit, Reno, NV, January, AIAA Paper 2007–1128, 2007.

[9]Mavriplis, D. J., "Solution of the Unsteady Discrete Adjoint for Three-Dimensional Problems on Dynamically Deforming Unstructured Meshes," Proceedings of the 46th Aerospace Sciences Meeting and Exhibit, Reno NV, AIAA Paper 2008–0727, 2008.

[10]Nielsen, E. J., Diskin, B., and Yamaleev, N., "Discrete Adjoint-Based Design Optimization of Unsteady Turbulent Flows on Dynamic Unstructured Grids," *AIAA Journal*, Vol. 48-6, June 2010, pp. 1195–1206.

[11]Nielsen, E. J., Lee-Rausch, E. M., and Jones, W. T., "Adjoint-Based Design of Rotors in a Noninertial Reference Frame," *Journal of Aircraft*, Vol. 47-2, March-April 2010, pp. 638–646.

[12]Mani, K. and Mavriplis, D. J., "Adjoint based sensitivity formulation for fully coupled unsteady aeroelasticity problems," *AIAA Journal*, Vol. 47, (8), August 2009, pp. 1902–1915.

[13]Mani, K. and Mavriplis, D. J., "Geometry Optimization in Three-Dimensional Unsteady Flow Problems using the Discrete Adjoint," 51st AIAA Aerospace Sciences Meeting, Grapevine, TX, AIAA Paper 2013-0662, January 2013.

[14]Mavriplis, D. J., "Discrete Adjoint-Based Approach for Optimization Problems on Three-Dimensional Unstructured Meshes," *AIAA Journal*, Vol. 45-4, April 2007, pp. 741–750.

[15]Mavriplis, D. J., "Solution of the Unsteady Discrete Adjoint for Three-Dimensional Problems on Dynamically Deforming Unstructured Meshes," Proceedings of the 46th AIAA Aerospace Sciences Meeting, Reno, NV, AIAA Paper 2008–0727, 2008.

[16]Spalart, P. R. and Allmaras, S. R., "A One-equation Turbulence Model for Aerodynamic Flows," *La Recherche Aérospatiale*, Vol. 1, 1994, pp. 5–21.

[17]Mavriplis, D. J., "Unstructured-Mesh Discretizations and Solvers for Computational Aerodynamics," *AIAA Journal*, Vol. 46-6, June 2008, pp. 1281–1298.

[18]Mavriplis, D. J., "Multigrid Strategies for Viscous Flow Solvers on Anisotropic Unstructured Meshes," *Journal of Computational Physics*, Vol. 145, (1), September 1998, pp. 141–165.

[19]Yang, Z. and Mavriplis, D. J., "A Mesh Deformation Strategy Optimized by the Adjoint Method on Unstructured Meshes," *AIAA Journal*, Vol. 45, (12), 2007, pp. 2885–2896.

[20]Mavriplis, D. J., Yang, Z., and Long, M., "Results using NSU3D for the first Aeroelastic Prediction Workshop," Proceedings of the 51st Aerospace Sciences Meeting and Exhibit, Grapevine TX, AIAA Paper 2013–0786, 2013.

[21]Schuster, D. M., Chwalowski, P., Heeg, J., and Wieseman, C. D., "Summary of Data and Findings from the First Aeroelastic Prediction Workshop," Seventh International Conference on Computational Fluid Dynamics (ICCFD7), July 9-13 2012.

[22]Kumar, A. A., Vishwamurthy, S. R., and Ganguli, R., "Correlation of helicopter rotor aeroelasticresponse with HART-II wind tunnel test data," *Aircraft Engineering and Aerospace Technology: An International Journal*, Vol. 82, (4), 2010, pp. 237–248.

[23]Yu, Y. H., Tung, C., van der Wall, B., Pausder, H.-J., Burley, C., Brooks, T., Beaumier, P., Delrieux, Y., Mercker, E., and Pengel, K., "The HART-II Test: Rotor Wakes and Aeroacoustics with Higher-Harmonic Pitch Control (HHC) Inputs -The Joint German/French/Dutch/US Project-," 58th American Helicopter Society Annual Forum, Montreal, Canada, June 11–13 2002.

[24]Chopra, I. and Bir, G., "University of Maryland Advanced Rotor Code: UMARC," American Helicopter Society Aeromechanics Specialists Conference, January 1994.

[25]Heckmann, A. Otter, M., Dietz, S., and Lopez, J. D., "The DLR FlexibleBodies Library to Model Large Motions of Beams and of flexible bodies exported from finite element programs," Modelica, September 4–5 2006.

[26]Smith, M. J., Lim, J. W., van der Wall, B. G., Baeder, J. D., Bierdron, R. T., Boyd Jr., D. D., Jayaraman, B., Junk, S. N., and Min, B.-Y., "Adjoint-based Unsteady Airfoil Design Optimization with application to Dynamic Stall," 68th American Helicopter Society Annual Forum, Fort Worth, TX, May 1–3 2012.

[27]Zhu, C., Byrd, R. H., Lu, P., and Nocedal, J., "L-BFGS-B - FORTRAN Subroutines for Large-scale Bound Constrained Optimization," Technical report, Department of Electrical Engineering and Computer Science, December 31 1994.